Featured in Physics

Three-Dimensional Moiré Crystal in Ultracold Atomic Gases

Ce Wang,[1] Chao Gao,[2,3,*] Jing Zhang,[4,5] Hui Zhai,[6,5] and Zhe-Yu Shi[7,†]
[1]School of Physics Science and Engineering, Tongji University, Shanghai 200092, China
[2]Department of Physics, Zhejiang Normal University, Jinhua 321004, China
[3]Key Laboratory of Optical Information Detection and Display Technology of Zhejiang, Zhejiang Normal University, Jinhua 321004, China
[4]State Key Laboratory of Quantum Optics and Quantum Optics Devices, Institute of Opto-Electronics, Collaborative Innovation Center of Extreme Optics, Shanxi University, Taiyuan, China
[5]Hefei National Laboratory, Hefei 230088, China
[6]Institute for Advanced Study, Tsinghua University, Beijing 100084, China
[7]State Key Laboratory of Precision Spectroscopy, East China Normal University, Shanghai 200062, China

(Received 11 May 2024; accepted 9 September 2024; published 15 October 2024)

The work intends to extend the moiré physics to three dimensions. Three-dimensional moiré patterns can be realized in ultracold atomic gases by coupling two spin states in spin-dependent optical lattices with a relative twist, a structure currently unachievable in solid-state materials. We give the commensurate conditions under which the three-dimensional moiré pattern features a periodic structure termed a three-dimensional moiré crystal. We emphasize a key distinction of three-dimensional moiré physics: In three dimensions, the twist operation generically does not commute with the rotational symmetry of the original lattice, unlike in two dimensions, where these two always commute. Consequently, the moiré crystal can exhibit a crystalline structure that differs from the original underlying lattice. We demonstrate that twisting a simple cubic lattice can generate various crystal structures. This capability of altering crystal structures by twisting offers a broad range of tunability for three-dimensional band structures.

DOI: 10.1103/PhysRevLett.133.163401

Large-scale moiré patterns emerge when two identical two-dimensional structures are overlaid with an offset. During recent years, studies of double-layered two-dimensional materials, such as twisted bilayer graphenes [1–6], twisted transition metal dichalcogenides heterostructures [7,8], and twisted cuprates [9,10], reveal that moiré patterns can substantially alter the electronic properties of the material. Many extraordinary phenomena, including flat bands [11,12], unconventional superconductivity [13–15], ferromagnetism [16,17], fractional Chern insulator [18–23], and fractional quantum anomalous Hall effect [24–27], have been predicted and discovered through creating moiré patterns in two-dimensional materials by twisting. The growing interest in twisted bilayer materials has developed a new field in condensed matter physics known as twistronics [28,29].

The impact of twistronics goes beyond condensed matter physics. For instance, a moiré superlattice has been achieved in photonic crystals [30–33] and optical lattices [34], paving the way for studying moiré physics in electromagnetic waves and ultracold atoms. Remarkably, the recent experimental realization of a two-dimensional moiré lattice in ultracold atomic gases utilizes the two internal states (spins) of atoms instead of two spatially separated layers [34,35]. In the experiment, ultracold ^{87}Rb atoms are loaded in two spin-dependent two-dimensional optical lattices with a relative twisted angle. The wavelengths of these two optical lattices are carefully selected such that each lattice only couples to one of the two spin states of a ^{87}Rb atom and is transparent to the other spin component. Therefore, although atoms with different spins coexist in the same space, their lattice potentials can be viewed as two independent layers, and an external microwave-induced coupling between the two spin states can play the role of interlayer tunneling. In this way, a moiré superlattice can be realized in an optical lattice setting, leading to an intriguing new phase observed between the conventional superfluid and Mott insulator transition [34].

This Letter proposes that this scheme of realizing moiré physics in ultracold atoms can be generalized to three dimensions. The flexibility in an ultracold atom apparatus allows twisting two sets of spin-dependent three-dimensional optical lattices along a generic axis $\mathbf{L}$ (not any of the principle axes of the original lattice) at a generic angle θ. Hence, it can create a three-dimensional moiré crystal when $\mathbf{L}$ and θ satisfy the commensurate condition discussed below. This generalization promotes moiré physics from two dimensions to three, presenting numerous new possibilities and opening up a new avenue in twistronics.

*Contact author: gaochao@zjnu.edu.cn
†Contact author: zyshi@lps.ecnu.edu.cn

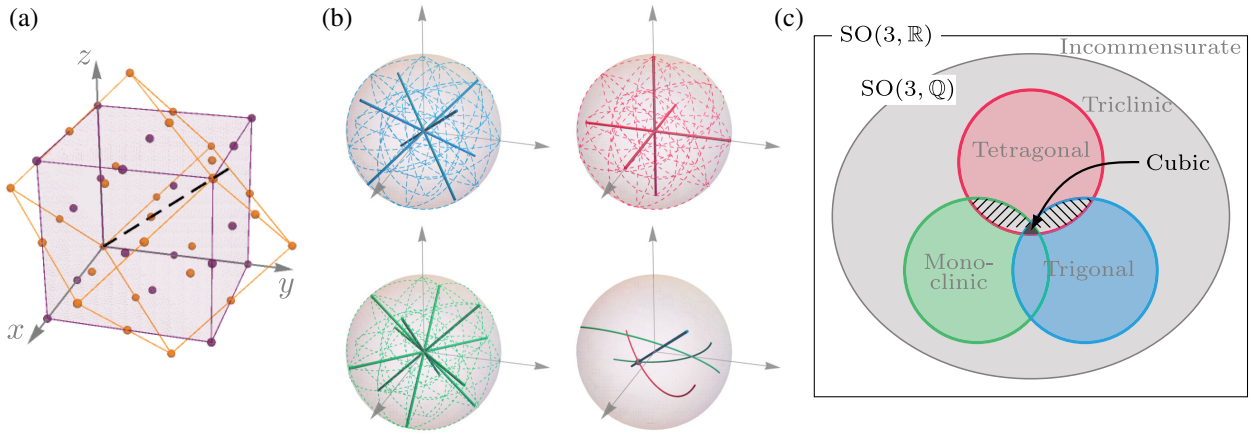

FIG. 1. (a) Schematic of an example of a three-dimensional moiré crystal. Two sets of cubic optical lattices represented by the purple and yellow dots are twisted along the body diagonal (111) direction (dashed line). (b) Three-dimensional twists under which the moiré crystal exhibits different rotational symmetry. Each rotation in SO(3) is represented by a point $\mathbf{r} = |\mathbf{r}|\hat{e}_{\mathbf{r}}$ within a ball of radius π. Here, $\hat{e}_{\mathbf{r}}$ represents the twisting axes, and $|\mathbf{r}|$ is the twist angle. The blue, red, and green lines indicate twists where the moiré crystals have C_3, C_4, or C_2 symmetry, respectively. The solid lines are positioned along the cubic lattice's symmetry axes. Twists belonging to these lines thus preserve the corresponding rotational symmetries. Additionally, twists represented by the dashed curves also lead to rotationally symmetric moiré crystals. This is because every twist R on a dashed curve may be transformed into a twist R' on a solid line by $R = R'g$, where $g \in O$. The lower right panel illustrates that the green line can intersect with the blue line, and these three lines can intersect at a single point. Twists represented by these intersection points possess multiple rotational symmetries. (c) The Venn diagram describing the crystal systems of different twists is presented in (b). The red, green, and blue areas represent the tetragonal, monoclinic, and trigonal crystal systems of a moiré crystal generated by the respective twists in (b). The black area represents the cubic moiré crystal generated by the intersection of these lines with different colors. Areas marked by dashed lines are empty sets. The gray area represents a triclinic crystal system with no rotational symmetry.

Here, we highlight a fundamental difference between the moiré physics in two and three dimensions. The difference stems from the non-Abelian nature of the SO(3) rotation group, as opposed to the Abelian SO(2) group. A two-dimensional twist, i.e., an element in SO(2), always commutes with the rotation symmetry of the original two-dimensional lattice, such as the C_4 rotation of a square lattice. Consequently, the moiré patterns of twisted bilayer square lattices always retain the exact C_4 symmetry. In contrast, a three-dimensional twist belonging to the non-Abelian SO(3) group generally does not commute with the rotation symmetry of the original three-dimensional lattice. As a result, a three-dimensional twist can disrupt the rotational symmetry of the original lattice, resulting in a distinct point group symmetry for the three-dimensional moiré crystal. This property allows a wide range of crystal structures to be generated by twisting the same lattice. It is worth mentioning that there have been previous studies of the moiré effect on three-dimensional solid-state systems [36–39]. However, these studies focus on systems of stacked multiple layers of twisted two-dimensional materials. Thus, accessible rotations in these systems are intrinsically two dimensional and are different from the moiré crystals considered in this Letter.

Physical model—A three-dimensional moiré crystal can be described by the following Hamiltonian of ultracold atoms with two spin components:

$$H = \begin{pmatrix} \frac{\mathbf{p}^2}{2m_0} + V_A + \frac{\delta}{2} & \Omega \\ \Omega & \frac{\mathbf{p}^2}{2m_0} + V_B - \frac{\delta}{2} \end{pmatrix}, \tag{1}$$

where m_0 is the mass of atoms and $\mathbf{p}$ is the momentum, Ω represents the coupling between two spin states with a detuning δ, and $V_{A,B}$ are the optical lattice potentials for the two spin states, respectively. For illustrative purposes, we consider a three-dimensional cubic lattice, where $V_A(\mathbf{r})$ is written as

$$V_A(\mathbf{r}) = V[\sin^2(\pi x) + \sin^2(\pi y) + \sin^2(\pi z)]. \tag{2}$$

Here, V stands for the lattice depth, and the recoil momentum has been taken to be π for simplicity. The optical lattice potential $V_B(\mathbf{r})$ is twisted with respect to $V_A(\mathbf{r})$ by a three-dimensional rotation. This is characterized by a rotation matrix $R \in \mathrm{SO}(3)$ and a displacement $\mathbf{d} \in \mathbb{R}^3$ as follows:

$$V_B(R\mathbf{r} + \mathbf{d}) = V_A(\mathbf{r}). \tag{3}$$

An example of the three-dimensional twisted moiré crystals is illustrated in Fig. 1(a).

Commensurate condition—Similar to the two-dimensional moiré systems, the moiré crystal appears only

when the rotation R satisfies certain commensurate conditions presented by the following theorem.

Theorem—The moiré pattern formed by overlapping two cubic lattices $V_A(\mathbf{r})$ and $V_B(\mathbf{r})$ forms a three-dimensional periodic lattice structure if and only if $R \in \mathrm{SO}(3,\mathbb{Q})$.

Here, $\mathrm{SO}(3,\mathbb{Q})$ is the set of all three-dimensional special orthogonal matrices with all entries being rational numbers [40]. In Supplemental Material, we show that every rotation matrix $R \in \mathrm{SO}(3,\mathbb{Q})$ can be uniquely parametrized by the axis of rotation $\mathbf{L} \equiv (l_1, l_2, l_3)$ and the rotation angle [41]

$$\theta = \arccos \frac{m^2 - n^2|\mathbf{L}|^2}{m^2 + n^2|\mathbf{L}|^2}. \tag{4}$$

Here, (l_1, l_2, l_3) are three integers with $\gcd(l_1, l_2, l_3) = 1$, and (m, n) are two integers with $\gcd(m, n) = 1$, where gcd stands for the greatest common divisor. Note that if we take the rotation axis $\mathbf{L} = (0, 0, 1)$, Eq. (4) becomes $\theta = \arccos[(m^2 - n^2)/(m^2 + n^2)]$, which coincides the commensurate condition for a twisted bilayer square lattice [34,52].

Proof—Note that all the lattice vectors of V_A form a three-dimensional Bravais lattice $\mathbb{Z}^3$; i.e., $V_A(\mathbf{r} + \mathbf{a}) = V_A(\mathbf{r})$ for all $\mathbf{r}$ if and only if $\mathbf{a} \in \mathbb{Z}^3$. Similarly, the lattice vectors of V_B form the set $R\mathbb{Z}^3 \equiv \{R\mathbf{a} | \mathbf{a} \in \mathbb{Z}^3\}$. One thus concludes that a vector $\mathbf{u}$ is a period of the moiré pattern if and only if $\mathbf{u} \in \mathbb{Z}^3 \cap R\mathbb{Z}^3$. Furthermore, the moiré pattern forms a three-dimensional lattice if and only if $\mathbb{Z}^3 \cap R\mathbb{Z}^3$ is a three-dimensional Bravais lattice.

To prove the theorem, we first show that if the rotation $R \in \mathrm{SO}(3,\mathbb{Q})$, then $\mathbb{Z}^3 \cap R\mathbb{Z}^3$ is a three-dimensional Bravais lattice. Consider vectors $R\hat{e}_1$, $R\hat{e}_2$, and $R\hat{e}_3$, where $\hat{e}_1 = (1, 0, 0)^T$, $\hat{e}_2 = (0, 1, 0)^T$, and $\hat{e}_3 = (0, 0, 1)^T$. These three vectors are linearly independent and have rational components if $R \in \mathrm{SO}(3,\mathbb{Q})$. One can then find integers n_i, such that all components of $n_i R\hat{e}_i$ are integers for each $i = 1, 2, 3$. This demonstrates that there exist three linearly independent vectors $n_i R\hat{e}_i \in \mathbb{Z}^3 \cap R\mathbb{Z}^3$, $i = 1, 2, 3$, and hence, $\mathbb{Z}^3 \cap R\mathbb{Z}^3$ is a three-dimensional Bravais lattice.

To prove the converse, we note that if $\mathbb{Z}^3 \cap R\mathbb{Z}^3$ is a three-dimensional Bravais lattice, there must exist three linearly independent integer vectors $\mathbf{u}_1, \mathbf{u}_2, \mathbf{u}_3 \in \mathbb{Z}^3 \cap R\mathbb{Z}^3$. Since $\mathbf{u}_1, \mathbf{u}_2, \mathbf{u}_3 \in R\mathbb{Z}^3$, there exist linearly independent integer vectors $\mathbf{v}_1$, $\mathbf{v}_2$, $\mathbf{v}_3$ such that $R(\mathbf{v}_1, \mathbf{v}_2, \mathbf{v}_3) = (\mathbf{u}_1, \mathbf{u}_2, \mathbf{u}_3)$. By writing $U = (\mathbf{u}_1, \mathbf{u}_2, \mathbf{u}_3)$ and $V = (\mathbf{v}_1, \mathbf{v}_2, \mathbf{v}_3)$, we thus have $R = UV^{-1} \in \mathrm{SO}(3,\mathbb{Q})$. This completes the proof.

The above proof shows that the periodicity of a moiré crystal is determined solely by the twist R; i.e., it is not affected by the displacement $\mathbf{d}$. Furthermore, it also provides an algorithm for calculating the unit cells and unit vectors of a three-dimensional moiré crystal. Note that a vector $\mathbf{u} \in \mathbb{Z}^3$ is a lattice vector if and only if there exists $\mathbf{v} \in \mathbb{Z}^3$ such that $R\mathbf{u} - \mathbf{v} = 0$. This equation can be viewed as a set of linear Diophantine equations for six integer variables $u_i, v_i, i = 1, 2, 3$, where u_i and v_i are the ith components of $\mathbf{u}$ and $\mathbf{v}$. Given that $R \in \mathrm{SO}(3,\mathbb{Q})$, it can be shown that every solution $(\mathbf{u}, \mathbf{v})^T$ can be uniquely expressed as an integer linear combination of three solutions $(\mathbf{u}_1, \mathbf{v}_1)^T$, $(\mathbf{u}_2, \mathbf{v}_2)^T$, and $(\mathbf{u}_3, \mathbf{v}_3)^T$. Therefore, $\mathbf{u}_1$, $\mathbf{u}_2$, $\mathbf{u}_3$ span the Bravais lattice $\mathbb{Z}^3 \cap R\mathbb{Z}^3$ and can be chosen as the unit lattice vectors of the three-dimensional moiré crystal [41].

Symmetry of moiré crystal—We now examine the crystal structures of moiré crystal by investigating its chiral point group, i.e., the set of all the proper rotational symmetries of the lattice. For simplicity, from this point forward, we will focus on the case where the displacement $\mathbf{d} = 0$, unless specified otherwise.

It is well known that the rotational symmetry of a cubic lattice V_A is described by the chiral octahedral group O. This group consists of 24 rotations [53]. As V_B is a lattice generated by twisting V_A by a rotation R, its chiral point group is then $ROR^{-1} \equiv \{RO_iR^{-1} | O_i \in O\}$. Consequently, the chiral point group of the moiré crystal can be directly inferred as $O \cap ROR^{-1}$.

At this point, we can further elaborate on the distinction between the moiré lattice in two and three dimensions. In two dimensions, because the rotation group $\mathrm{SO}(2,\mathbb{R})$ is Abelian, one has $RgR^{-1} \equiv g$ for any $g, R \in \mathrm{SO}(2,\mathbb{R})$. Therefore, $O \cap ROR^{-1} \equiv O$, and the moiré lattice always maintains the same rotational symmetry as the original lattice. In three dimensions, however, one generically has $RgR^{-1} \neq g$ because of the non-Abelian nature of $\mathrm{SO}(3,\mathbb{R})$. The chiral point group of a three-dimensional moiré crystal is thus different from that of the original lattice and, more crucially, can be tuned by choosing an appropriate twist R. In Fig. 1(b), we illustrate different classes of twists that lead to different rotation symmetries of the moiré crystals. We use a three-dimensional ball with radius π to represent all SO(3) rotation symmetry, where the direction $\hat{e}_{\mathbf{r}}$ of a given point denotes its rotation axis, and the length $|\mathbf{r}|$ denotes its rotation angle.

In the first plot, the blue lines represent all the twists that can lead to a C_3 symmetric moiré crystal belonging to the trigonal crystal system. Note that the blue solid lines contain all the rotations along the body diagonals such as the (1,1,1) direction. As these body diagonals are the C_3 axes of the original cubic lattice V_A, any rotation along one of these axes preserves the corresponding rotation symmetry. However, these rotations do not cover all the twists resulting in C_3 symmetry. We emphasize that two rotations R and R' should yield the same moiré crystal if $R = R'g$ for some g belonging to the chiral octahedral group, i.e., the rotation symmetries of V_A. This equivalence generates other dashed blue lines in the plot which cover all the rotations leading to moiré crystals with C_3 symmetry.

Similarly, in the other two plots of Fig. 1(b), we illustrate the twists that result in a moiré crystal with C_4 symmetry

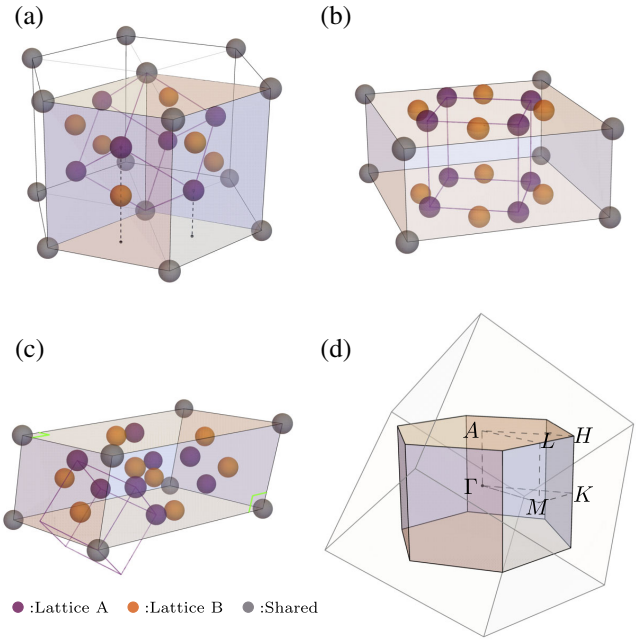

FIG. 2. (a)–(c) Lattice structures of twisted cubic lattices with different twisting axes $\mathbf{L}$ and twisting angle θ. (a) $\mathbf{L} = (1,1,1)$ and $\theta = \pi/3$ with $(m,n) = (3,1)$. (b) $\mathbf{L} = (0,0,1)$ and $\theta = \arccos\frac{3}{5}$ with $(m,n) = (2,1)$. (c) $\mathbf{L} = (1,1,0)$ and $\theta = \arccos\frac{7}{9}$ with $(m,n) = (4,1)$. They belong to the trigonal, tetragonal, and monoclinic crystal systems, respectively. The blue, red, and gray dots represent the lattice sites of lattice A, lattice B, and those shared by both lattices, respectively. The unit cell is denoted by the shaded prism. (d) The first Brillouin zone (shaded hexagonal prism) and high-symmetry points for the reciprocal lattice of the moiré crystal are presented in (a). The cube formed by the black edges represents the first Brillouin zone of the original cubic lattice A.

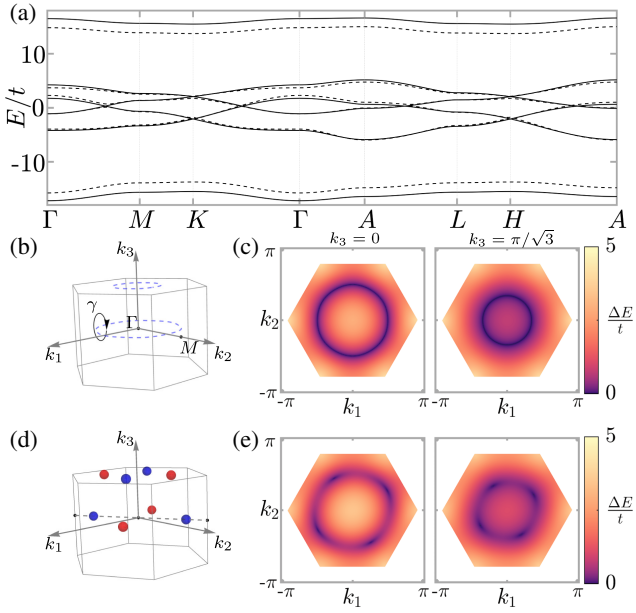

FIG. 3. (a) Band structures of the moiré crystal with twisting axes $\mathbf{L} = (1,1,1)$ and twisting angle $\theta = \pi/3$ with $(m,n) = (3,1)$, whose real-space structure is shown in Fig. 2(a). The displacements between V_A and V_B are $\mathbf{d} = (0,0,0)$ for solid lines, and $\mathbf{d} = (0,0.1,-0.1)$ for dashed lines. The calculations are based on the tight-binding approximation for Hamiltonian (1) with parameters $V = 6\pi^2/(2m_0)$, $\Omega = \pi^2/(2m_0)$, and $\delta = 0$, and t is the tight-binding tunneling coefficient for the square lattice. (b) Schematic plots showing two topological nodal lines for displacement $\mathbf{d} = (0,0,0)$ and (d) eight Weyl points for displacement $\mathbf{d} = (0,0.1,-0.1)$. The blue and red points indicate the positions for the Weyl points with Chern number $+1/-1$. (c) Band gaps $E_4(\mathbf{k}) - E_3(\mathbf{k})$ for displacement $\mathbf{d} = (0,0,0)$, and (e) $\mathbf{d} = (0,0.1,-0.1)$. Left, $k_3 = 0$ plane; right, $k_3 = \pi/\sqrt{3}$ plane. Note that the dark spots denote the positions of the gapless points.

(red lines) belonging to tetragonal crystal system, or C_2 symmetry (green lines) belonging to monoclinic crystal system, assuming no other rotational symmetry exists. The last plot of Fig. 1(b) gives examples of how a green line could intersect with a blue line, where the intersection points denote a twist resulting in both C_3 and C_2 symmetry, also belonging to the trigonal crystal system. Moreover, three lines of different colors can also intersect at the same point, representing a twist that can recover the cubic symmetry. Finally, other twists in $\mathrm{SO}(3,\mathbb{Q})$ that do not belong to the lines in Fig. 1(b) lead to a moiré crystal with no rotational symmetry, belonging to the triclinic class.

The classification of the moiré crystal systems is shown in Fig. 1(c) by the Venn diagram. Notably, a rich set of crystal structures, i.e., five out of a total of seven possible crystal systems in three dimensions, emerge through twisting two simple cubic lattices. In Fig. 2, we present three examples of different moiré crystals belonging to the trigonal, tetragonal, and monoclinic crystal systems, respectively. The gray points denote the lattice sites shared by the A and B lattices, clearly illustrating unit cells with diverse geometries.

Band structures—The ability to control the crystalline symmetry through three-dimensional twists offers increased flexibility for engineering band dispersion. Here, as a first demonstration of such a tunability in three dimensions, we focus on a specific rotation parametrized by twisting along $\mathbf{L} = (1,1,1)$ by $\theta = \pi/3$. The real-space moiré crystal structure is shown in Fig. 2(a), and its moiré Brillouin zone is depicted in Fig. 2(d). This is reminiscent of the Brillouin zone of many materials with symmetry-protected nodal lines or nodal points [54–60]. Therefore, it inspires us to examine the topological feature in this moiré crystal.

In Fig. 3, we plot the band structures of this moiré crystal under a tight-binding approximation [41,43,61,62]. Interestingly, it is discovered that the dispersion can support nontrivial gapless lines between the third and the fourth bands [41], as shown in Figs. 3(b) and 3(c). These two gapless lines in the $k_3 = 0$ and $k_3 = \pi/\sqrt{3}$ planes are topological nodal lines [45–49] protected by either the $\mathcal{PT}$

symmetry or the $\mathcal{M}\sigma_x$ symmetry simultaneously. Here, $\mathcal{P}$ represents the inversion against the origin, $\mathcal{T}$ represents the (spinless) time reversal operation, $\mathcal{M}$ stands for the reflection against the plane perpendicular to the body diagonal (111) direction, and σ_x is the spin-flip operation for the two hyperfine spins. Both symmetries are maintained when $\mathbf{d} = 0$. When we introduce a finite perturbation in $\mathbf{d}$, e.g., along the $(0, 1, -1)$ direction, both symmetries are simultaneously broken, which partially gaps the topological nodal lines and results in four pairs of gapless Weyl points [41,63,64], as shown in Figs. 3(d) and 3(e). These Weyl points all carry nonvanishing Chern numbers with $C = \pm 1$, suggesting they are stable against perturbations that preserve the lattice translation symmetries.

Conclusion and outlook—In summary, we propose to generalize the moiré physics to three dimensions. We present the commensurate condition for the moiré crystal and highlight that different crystal structures of the moiré pattern can be realized by twisting the same cubic lattice along different axes and angles. The specific features of three-dimensional moiré lattices will bring many opportunities for future research.

First, the complexity of the three-dimensional rotation group allows more flexible band engineering, which can lead to nontrivial band topologies or flat bands. In this Letter, we have shown the example of generating topological nodal lines and Weyl points through a three-dimensional twist. Yet, given the extensive parameter space of the $\mathrm{SO}(3, \mathbb{Q})$ group, more systematic studies of band structures are required for future investigations. Second, two-dimensional moiré systems can exhibit a variety of highly nontrivial correlation effects by introducing interactions [6,34,65–69]. Similar or even more sophisticated correlation effects could occur in three dimensions. Third, we have focused on commensurate crystals, while incommensurate twists can also reveal intriguing physics in three dimensions. Finally, we have discussed the potential for realizing a three-dimensional moiré crystal in ultracold atoms, and a similar realization may also be possible in photonic systems [70–72].

Acknowledgments—We thank Biao Lian, Zhong Wang, Zengming Meng, Jie Ren, Zhiwei Guo, Yizhou Liu, and Xingze Qiu for inspiring discussion. This work is supported by the National Natural Science Foundation of China under Grants No. 12204352 (C. W.), No. 12474493 (C. G.), No. 10274342 (C. G.), No. 12034011 (J. Z.), No. U23A6004 (J. Z. and H. Z.), and No. 12004115 (Z. Y. S.), the Innovation Program for Quantum Science and Technology under Grants No. 2021ZD0302003 (J. Z.) and No. 2021ZD0302005 (H. Z.), the National Key R&D Program of China Grant No. 2023YFA1406702 (H. Z.), the XPLORER grant (J. Z. and H. Z.), and the Natural Science Foundation of Zhejiang Province, China under Grants No. LR22A040001 (C. G.) and No. LY21A040004 (C. G.).

[1] Y. Cao, V. Fatemi, A. Demir, S. Fang, S. L. Tomarken, J. Y. Luo, J. D. Sanchez-Yamagishi, K. Watanabe, T. Taniguchi, E. Kaxiras, R. C. Ashoori, and P. Jarillo-Herrero, Nature (London) **556**, 80 (2018).
[2] Y. Cao, V. Fatemi, S. Fang, K. Watanabe, T. Taniguchi, E. Kaxiras, and P. Jarillo-Herrero, Nature (London) **556**, 43 (2018).
[3] M. Yankowitz, S. Chen, H. Polshyn, Y. Zhang, K. Watanabe, T. Taniguchi, D. Graf, A. F. Young, and C. R. Dean, Science **363**, 1059 (2019).
[4] X. Lu, P. Stepanov, W. Yang, M. Xie, M. A. Aamir, I. Das, C. Urgell, K. Watanabe, T. Taniguchi, G. Zhang, A. Bachtold, A. H. MacDonald, and D. K. Efetov, Nature (London) **574**, 653 (2019).
[5] E. Y. Andrei and A. H. MacDonald, Nat. Mater. **19**, 1265 (2020).
[6] L. Balents, C. R. Dean, D. K. Efetov, and A. F. Young, Nat. Phys. **16**, 725 (2020).
[7] Y. Tang, L. Li, T. Li, Y. Xu, S. Liu, K. Barmak, K. Watanabe, T. Taniguchi, A. H. MacDonald, J. Shan *et al.*, Nature (London) **579**, 353 (2020).
[8] E. C. Regan, D. Wang, C. Jin, M. I. B. Utama, B. Gao, X. Wei, S. Zhao, W. Zhao, Z. Zhang, K. Yumigeta *et al.*, Nature (London) **579**, 359 (2020).
[9] O. Can, T. Tummuru, R. P. Day, I. Elfimov, A. Damascelli, and M. Franz, Nat. Phys. **17**, 519 (2021).
[10] S. F. Zhao, X. Cui, P. A. Volkov, H. Yoo, S. Lee, J. A. Gardener, A. J. Akey, R. Engelke, Y. Ronen, R. Zhong *et al.*, Science **382**, 1422 (2023).
[11] R. Bistritzer and A. H. MacDonald, Proc. Natl. Acad. Sci. U.S.A. **108**, 12233 (2011).
[12] G. Tarnopolsky, A. J. Kruchkov, and A. Vishwanath, Phys. Rev. Lett. **122**, 106405 (2019).
[13] F. Wu, A. H. MacDonald, and I. Martin, Phys. Rev. Lett. **121**, 257001 (2018).
[14] H. Isobe, N. F. Q. Yuan, and L. Fu, Phys. Rev. X **8**, 041041 (2018).
[15] B. Lian, Z. Wang, and B. A. Bernevig, Phys. Rev. Lett. **122**, 257002 (2019).
[16] A. L. Sharpe, E. J. Fox, A. W. Barnard, J. Finney, K. Watanabe, T. Taniguchi, M. A. Kastner, and D. Goldhaber-Gordon, Science **365**, 605 (2019).
[17] J.-X. Lin, Y.-H. Zhang, E. Morissette, Z. Wang, S. Liu, D. Rhodes, K. Watanabe, T. Taniguchi, J. Hone, and J. I. A. Li, Science **375**, 437 (2022).
[18] E. M. Spanton, A. A. Zibrov, H. Zhou, T. Taniguchi, K. Watanabe, M. P. Zaletel, and A. F. Young, Science **360**, 62 (2018).
[19] Y. Zeng, Z. Xia, K. Kang, J. Zhu, P. Knüppel, C. Vaswani, K. Watanabe, T. Taniguchi, K. F. Mak, and J. Shan, Nature (London) **622**, 69 (2023).
[20] H. Yu, M. Chen, and W. Yao, Natl. Sci. Rev. **7**, 12 (2020).
[21] N. Morales-Durán, N. Wei, J. Shi, and A. H. MacDonald, Phys. Rev. Lett. **132**, 096602 (2024).
[22] C. Wang, X.-W. Zhang, X. Liu, Y. He, X. Xu, Y. Ran, T. Cao, and D. Xiao, Phys. Rev. Lett. **132**, 036501 (2024).
[23] Z. Liu and E. J. Bergholtz, Recent developments in fractional Chern insulators, in *Encyclopedia of Condensed Matter Physics* (Elsevier, New York, 2024), pp. 515–538.

[24] J. Cai, E. Anderson, C. Wang, X. Zhang, X. Liu, W. Holtzmann, Y. Zhang, F. Fan, T. Taniguchi, K. Watanabe, Y. Ran, T. Cao, L. Fu, D. Xiao, W. Yao, and X. Xu, Nature (London) **622**, 63 (2023).

[25] H. Park, J. Cai, E. Anderson, Y. Zhang, J. Zhu, X. Liu, C. Wang, W. Holtzmann, C. Hu, Z. Liu, T. Taniguchi, K. Watanabe, J.-H. Chu, T. Cao, L. Fu, W. Yao, C.-Z. Chang, D. Cobden, D. Xiao, and X. Xu, Nature (London) **622**, 74 (2023).

[26] F. Xu, Z. Sun, T. Jia, C. Liu, C. Xu, C. Li, Y. Gu, K. Watanabe, T. Taniguchi, B. Tong, J. Jia, Z. Shi, S. Jiang, Y. Zhang, X. Liu, and T. Li, Phys. Rev. X **13**, 031037 (2023).

[27] Z. Lu, T. Han, Y. Yao, A. P. Reddy, J. Yang, J. Seo, K. Watanabe, T. Taniguchi, L. Fu, and L. Ju, Nature (London) **626**, 759 (2024).

[28] S. Carr, D. Massatt, S. Fang, P. Cazeaux, M. Luskin, and E. Kaxiras, Phys. Rev. B **95**, 075420 (2017).

[29] S. Carr, S. Fang, and E. Kaxiras, Nat. Rev. Mater. **5**, 748 (2020).

[30] P. Wang, Y. Zheng, X. Chen, C. Huang, Y. V. Kartashov, L. Torner, V. V. Konotop, and F. Ye, Nature (London) **577**, 42 (2020).

[31] B. Lou, B. Wang, J. A. Rodríguez, M. Cappelli, and S. Fan, Sci. Adv. **8**, eadd4339 (2022).

[32] H. Tang, B. Lou, F. Du, M. Zhang, X. Ni, W. Xu, R. Jin, S. Fan, and E. Mazur, Sci. Adv. **9**, eadh8498 (2023).

[33] H.-Y. Luan, Y.-H. Ouyang, Z.-W. Zhao, W.-Z. Mao, and R.-M. Ma, Nature (London) **624**, 282 (2023).

[34] Z. Meng, L. Wang, W. Han, F. Liu, K. Wen, C. Gao, P. Wang, C. Chin, and J. Zhang, Nature (London) **615**, 231 (2023).

[35] A. González-Tudela and J. I. Cirac, Phys. Rev. A **100**, 053604 (2019).

[36] F. Wu, R.-X. Zhang, and S. Das Sarma, Phys. Rev. Res. **2**, 022010(R) (2020).

[37] Z. Song, X. Sun, and L.-W. Wang, Phys. Rev. B **103**, 245206 (2021).

[38] L. Xian, A. Fischer, M. Claassen, J. Zhang, A. Rubio, and D. M. Kennes, Nano Lett. **21**, 7519 (2021).

[39] X. Lu, B. Xie, Y. Yang, Y. Zhang, X. Kong, J. Li, F. Ding, Z.-J. Wang, and J. Liu, Phys. Rev. Lett. **132**, 056601 (2024).

[40] We note that previously we have implicitly assumed that we consider matrices on the field of real numbers. Thus, to avoid confusion, we shall denote SO(3) by $\mathrm{SO}(3,\mathbb{R})$ hereafter.

[41] See Supplemental Material at http://link.aps.org/supplemental/10.1103/PhysRevLett.133.163401 for parametrization of $\mathrm{SO}(3,\mathbb{R})$ different rotation formalisms, and details on band structures, which includes Refs. [42–51].

[42] C. C. MacDuffee, *The Theory of Matrices* (Springer Science & Business Media, New York, 2012), Vol. 5.

[43] W. Zwerger, J. Opt. B **5**, S9 (2003).

[44] X. Wan, A. M. Turner, A. Vishwanath, and S. Y. Savrasov, Phys. Rev. B **83**, 205101 (2011).

[45] A. A. Burkov, M. D. Hook, and L. Balents, Phys. Rev. B **84**, 235126 (2011).

[46] C. Fang, Y. Chen, H.-Y. Kee, and L. Fu, Phys. Rev. B **92**, 081201(R) (2015).

[47] R. Yu, H. Weng, Z. Fang, X. Dai, and X. Hu, Phys. Rev. Lett. **115**, 036807 (2015).

[48] C. Fang, H. Weng, X. Dai, and Z. Fang, Chin. Phys. B **25**, 117106 (2016).

[49] Q. Xu, R. Yu, Z. Fang, X. Dai, and H. Weng, Phys. Rev. B **95**, 045136 (2017).

[50] R. Okugawa and S. Murakami, Phys. Rev. B **96**, 115201 (2017).

[51] J. Li, H. Wang, and H. Pan, Phys. Rev. B **104**, 235136 (2021).

[52] C. Huang, F. Ye, X. Chen, Y. V. Kartashov, V. V. Konotop, and L. Torner, Sci. Rep. **6**, 32546 (2016).

[53] They are three C_4 axes along the three perpendicular edges [such as the (100) direction] of the cube, four C_3 axes along the body diagonals [such as (111)], and six C_2 axes along the face diagonals [such as (110)].

[54] M. Hirayama, R. Okugawa, S. Ishibashi, S. Murakami, and T. Miyake, Phys. Rev. Lett. **114**, 206401 (2015).

[55] X. Zhang, L. Jin, X. Dai, and G. Liu, J. Phys. Chem. Lett. **8**, 4814 (2017).

[56] Q. S. Wu, C. Piveteau, Z. Song, and O. V. Yazyev, Phys. Rev. B **98**, 081115(R) (2018).

[57] G. Hua, S. Nie, Z. Song, R. Yu, G. Xu, and K. Yao, Phys. Rev. B **98**, 201116(R) (2018).

[58] Y.-H. Chan, B. Kilic, M. M. Hirschmann, C.-K. Chiu, L. M. Schoop, D. G. Joshi, and A. P. Schnyder, Phys. Rev. Mater. **3**, 124204 (2019).

[59] Z.-Y. Wang, X.-C. Cheng, B.-Z. Wang, J.-Y. Zhang, Y.-H. Lu, C.-R. Yi, S. Niu, Y. Deng, X.-J. Liu, S. Chen *et al.*, Science **372**, 271 (2021).

[60] W.-Y. He, S. Zhang, and K. T. Law, Phys. Rev. A **94**, 013606 (2016).

[61] I. Bloch, J. Dalibard, and W. Zwerger, Rev. Mod. Phys. **80**, 885 (2008).

[62] The codes are available at https://github.com/physicswangce/3D-Moire-Crystal.

[63] B. Yan and C. Felser, Annu. Rev. Condens. Matter Phys. **8**, 337 (2017).

[64] N. P. Armitage, E. J. Mele, and A. Vishwanath, Rev. Mod. Phys. **90**, 015001 (2018).

[65] K. Kim, A. DaSilva, S. Huang, B. Fallahazad, S. Larentis, T. Taniguchi, K. Watanabe, B. J. LeRoy, A. H. MacDonald, and E. Tutuc, Proc. Natl. Acad. Sci. U.S.A. **114**, 3364 (2017).

[66] Y. Shimazaki, I. Schwartz, K. Watanabe, T. Taniguchi, M. Kroner, and A. Imamoğlu, Nature (London) **580**, 472 (2020).

[67] L. Wang, E.-M. Shih, A. Ghiotto, L. Xian, D. A. Rhodes, C. Tan, M. Claassen, D. M. Kennes, Y. Bai, B. Kim, K. Watanabe, T. Taniguchi, X. Zhu, J. Hone, A. Rubio, A. N. Pasupathy, and C. R. Dean, Nat. Mater. **19**, 861 (2020).

[68] G. Chen, A. L. Sharpe, E. J. Fox, Y.-H. Zhang, S. Wang, L. Jiang, B. Lyu, H. Li, K. Watanabe, T. Taniguchi, Z. Shi, T. Senthil, D. Goldhaber-Gordon, Y. Zhang, and F. Wang, Nature (London) **579**, 56 (2020).

[69] X.-W. Luo and C. Zhang, Phys. Rev. Lett. **126**, 103201 (2021).

[70] L. Lu, Z. Wang, D. Ye, L. Ran, L. Fu, J. D. Joannopoulos, and M. Soljačić, Science **349**, 622 (2015).

[71] Y. Zhang, F. Zhang, Z. Yan, Q. Ma, X. Li, Y. Huang, and J. A. Rogers, Nat. Rev. Mater. **2**, 1 (2017).

[72] Y. Yang, Z. Gao, H. Xue, L. Zhang, M. He, Z. Yang, R. Singh, Y. Chong, B. Zhang, and H. Chen, Nature (London) **565**, 622 (2019).
[73] W. Setyawan and S. Curtarolo, Comput. Mater. Sci. **49**, 299 (2010).
[74] Q. Wu, A. A. Soluyanov, and T. Bzdušek, Science **365**, 1273 (2019).
[75] Any finite displacement $\mathbf{d}$ will generically break these symmetries simultaneously. Yet, we choose the (1,1,0) direction because it is the C_2 axis of the monoclinic moiré crystal. Therefore, the displacements along this direction preserve the C_2 rotational symmetry of the lattice, which helps the search of remaining Weyl nodes on the high-symmetry axis numerically.

End Matter

Appendix—In this section, we report the band structures and topologies of the other two moiré crystals that are shown in Fig. 2. The results reveal that nontrivial topological features, specifically, nodal lines and Weyl points, can also exist in such lattices.

The monoclinic moiré crystal In this subsection, we analyze the band structure and topology of the monoclinic moiré crystal with parametrization $(m, n, l_1, l_2, l_3) = (4, 1, 1, 1, 0)$.

The real-space unit cell of this lattice is shown in Fig. 2(c) of the main text. In Fig. 4, we plot the first Brillouin zone and the band structure of this lattice without displacement, i.e., $\mathbf{d} = (0, 0, 0)$. There are 18 bands in total, as both lattice A and lattice B contribute nine lattice sites to one moiré crystal unit cell.

We find that the monoclinic lattice can also support topological nodal lines protected by crystalline symmetry just like the trigonal lattice. For example, in Figs. 5(a)–5(d), we plot the gapless lines between the 13th and 14th bands in the Brillouin zone, i.e., the solutions to the equation $E_{14}(\mathbf{k}) - E_{13}(\mathbf{k}) = 0$. We find two types of nodal lines as indicated by the blue dashed and the red solid lines in Figs. 5(a) and 5(c). Both types are protected by the $\mathcal{PT}$ symmetry. Additionally, the blue dashed (red solid) nodal lines are also protected by the $\mathcal{M}_1\sigma_x$ ($\mathcal{M}_3\sigma_x$) symmetry. Here, $\mathcal{M}_i (i = 1, 2, 3)$ represents the reflection operation with respect to $P_i = \{\mathbf{r} \in \mathbb{R}^3 | \mathbf{b}_i \cdot \mathbf{r} = 0\}$, i.e., the plane perpendicular to $\mathbf{b}_i$ and go through the origin.

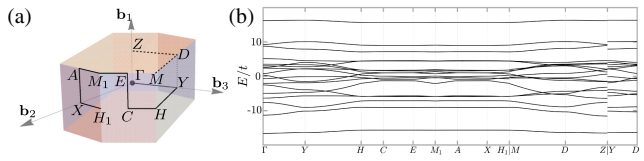

FIG. 4. (a) The first Brillouin zone (shaded hexagonal prism) and high-symmetry points for the monoclinic moiré crystal parametrized by $(m, n, l_1, l_2, l_3) = (4, 1, 1, 1, 0)$. We adopt the same convention as Ref. [73]. The unit reciprocal vectors are represented by $\mathbf{b}_1 = [(4\pi/9), -(4\pi/9), -(2\pi/9)]$, $\mathbf{b}_2 = [(8\pi/9), (10\pi/9), -(4\pi/9)]$, and $\mathbf{b}_3 = [(2\pi/9), -(2\pi/9), (8\pi/9)]$, respectively. (b) Band structure of the monoclinic lattice based on tight-binding approximation. The parameters V, Ω, and δ are identical to the ones used in the previous calculation of the trigonal lattice. The displacement $\mathbf{d}$ is set to zero.

It is worth noting that the two types of nodal lines may intersect with each other. For example, one can see that the red solid nodal circles on the $k_3 = \sqrt{2}\pi/3$ plane [i.e., the right purple plane in Fig. 5(c)] intersect the right blue-dashed semiarc in Fig. 5(a). These intersections of nodal

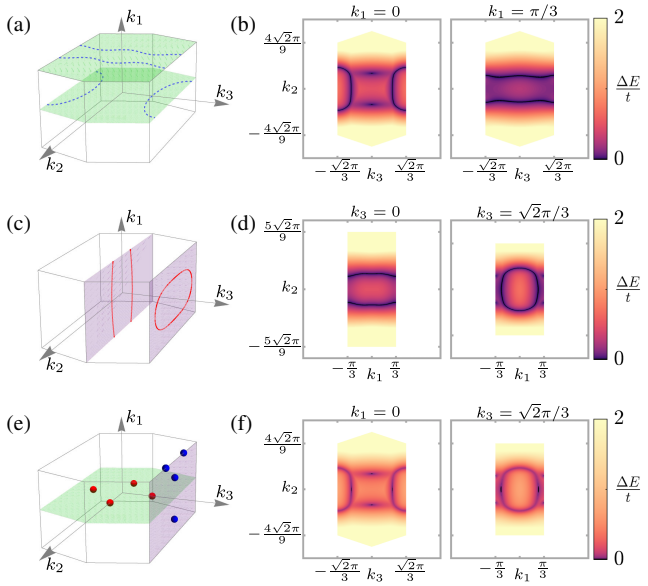

FIG. 5. Plots showing the topological nodal lines for $\mathbf{d} = (0, 0, 0)$ [(a)-(d)] and the Weyl points for $\mathbf{d} = (0.01, 0.01, 0)$ [(e), (f)] between the 13th and the 14th bands of the monoclinic moiré crystal parametrized by $(m, n, l_1, l_2, l_3) = (4, 1, 1, 1, 0)$. (a) Schematic plots showing the three nodal lines (blue dashed) on the high-symmetry (green) planes of the $\mathcal{M}_1\sigma_x$ symmetry. (b) Band gaps $E_{14}(\mathbf{k}) - E_{13}(\mathbf{k})$ on the high-symmetry planes displayed in (a). Note that the dark lines represent the nodal lines. (c) Schematic plots showing the three nodal lines (red solid) on the high-symmetry (purple) planes of the $\mathcal{M}_2\sigma_x$ symmetry. (d) Band gaps $E_{14}(\mathbf{k}) - E_{13}(\mathbf{k})$ on the high-symmetry planes displayed in (c). The dark lines represent the nodal lines. (e) Schematic plots showing the eight Weyl points. The blue and red points indicate the positions of Weyl points with Chern number $+1/-1$. Note that all the Weyl points are on the high-symmetry axes corresponding to certain rotational symmetry, e.g., the C_2 rotation along the (1,1,0) axis. These symmetries are not essential to protect these Weyl points, but help us locating their positions numerically. (f) Band gaps $E_{14}(\mathbf{k}) - E_{13}(\mathbf{k})$ on the high-symmetry planes displayed in (e). The dark points indicate the actual positions of the eight Weyl points.

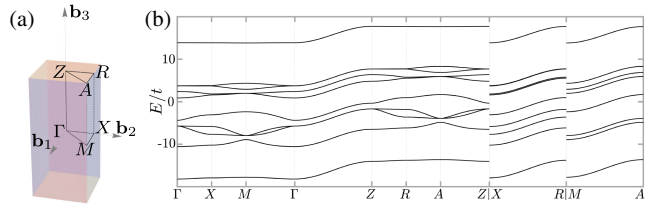

FIG. 6. (a) The first Brillouin zone (shaded rectangular cuboid) and high-symmetry points for the tetragonal moiré crystal parametrized by $(m, n, l_1, l_2, l_3) = (2, 1, 0, 0, 1)$. We adopt the same convention as Ref. [73]. The unit reciprocal vectors are represented by $\mathbf{b}_1 = [(4\pi/5), (2\pi/5), 0]$, $\mathbf{b}_2 = [-(2\pi/5), (4\pi/5), 0]$, and $\mathbf{b}_3 = (0, 0, 2\pi)$, respectively. (b) Band structure of the tetragonal lattice based on tight-binding approximation. The parameters V, Ω, and δ are identical to the ones used in previous calculations of the trigonal and monoclinic lattices. The displacement $\mathbf{d}$ is set to zero.

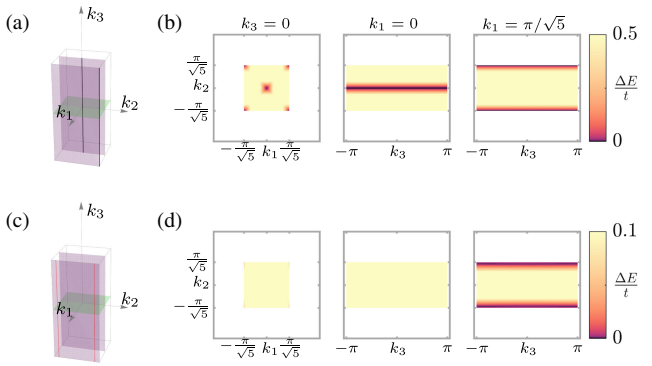

FIG. 7. Plots showing the nodal lines protected by the non-Abelian $D_4 \times \mathbb{Z}_2$ symmetry for $\mathbf{d} = (0, 0, 0)$ [(a),(b)] and the topological nodal lines for $\mathbf{d} = (0.16, 0.08, 0)$ [(c),(d)] between the third and the fourth bands of the tetragonal moiré crystal parametrized by $(m, n, l_1, l_2, l_3) = (2, 1, 0, 0, 1)$. (a) Schematic plots showing the two nodal lines (black solid) on the high-symmetry axes of the $D_4 \times \mathbb{Z}_2$ symmetry. The two degenerate eigenstates on these lines form a two-dimensional irreducible representation of the group. (b) Band gaps $E_4(\mathbf{k}) - E_3(\mathbf{k})$ on the high-symmetry planes displayed in (a). Note that the dark lines represent the nodal lines. (c) Schematic plots showing the two topological nodal lines (red solid) on the high-symmetry (purple) plane of the $\mathcal{M}_1\sigma_x$ symmetry. (d) Band gaps $E_4(\mathbf{k}) - E_3(\mathbf{k})$ on the high-symmetry planes displayed in (c). The dark lines represent the nodal lines.

lines do not fall in the paradigm of the "tenfold-way" classification of band topologies based on K theory, but are still topologically nontrivial in the sense of non-Abelian band topology [74]. Consequently, even perturbation in the parameters that respect all the system symmetry can break an intersection between two nodal lines of the 13th and 14th bands. Yet, the intersection point does not disappear but is transferred to other bands. For example, two nodal lines of the 14th and 15th bands can become intersecting after the perturbation, which leaves the total number of intersection points conserved in the entire band structure [74].

Similar to the trigonal case studied previously, these symmetry-protected nodal lines may be gapped by introducing a finite displacement between the A and B lattices. For instance, a finite $\mathbf{d}$ along the direction (1,1,0) breaks the $\mathcal{M}_1\sigma_x$, the $\mathcal{M}_3\sigma_x$, and the $\mathcal{PT}$ symmetries simultaneously [75], and hence should gap all the nodal lines. Indeed, in Figs. 5(e) and 5(f), we see that a small displacement in this direction gaps all the nodal lines except a few nodal points, i.e., the Weyl points with nonvanishing Chern numbers.

The tetragonal moiré crystal In this subsection, we analyze the band structure and topology of the tetragonal moiré crystal with parametrization $(m, n, l_1, l_2, l_3) = (2, 1, 0, 0, 1)$.

The real-space unit cell of this lattice is shown in Fig. 2(b) of the main text. In Fig. 6, we plot the first Brillouin zone and the band structure of this lattice without displacement, i.e., $\mathbf{d} = (0, 0, 0)$. There are ten bands in total, as both lattice A and lattice B contribute five lattice sites to one moiré crystal unit cell.

The tetragonal moiré crystal can also support nodal line structures with $\mathbf{d} = (0, 0, 0)$. For example, as shown in Figs. 7(a) and 7(b), there exist two nodal lines (black solid) along the ΓZ and the MA axes between the third and the fourth bands. However, it is worth noting that these two nodal lines are not topological. They are protected by the non-Abelian crystalline symmetry of the lattice. To see this, note that besides the obvious C_4 symmetry, the lattice also contains a reflection symmetry $\mathcal{M}_3$ and a combined reflection and spin-flip symmetry $\mathcal{M}_1\sigma_x$. Similar to the previous subsection, here $\mathcal{M}_i (i = 1, 2, 3)$ represents the reflection operation with respect to $P_i = \{\mathbf{r} \in \mathbb{R}^3 | \mathbf{b}_i \cdot \mathbf{r} = 0\}$, i.e., the plane perpendicular to $\mathbf{b}_i$ and go through the origin. The C_4 rotational symmetry together with the $\mathcal{M}_3$ and the $\mathcal{M}_1\sigma_x$ generate a symmetry group isomorphic to $D_4 \times \mathbb{Z}_2$. This group is non-Abelian, and thus allows high-dimensional irreducible representations at the corresponding high-symmetry axes of the Brillouin zone, i.e., the ΓZ and the MA axes. The nodal lines at these two axes between the third and the fourth bands are thus a consequence of the two-dimensional irreducible representations of the non-Abelian $D_4 \times \mathbb{Z}_2$ group.

The $D_4 \times \mathbb{Z}_2$ can be broken by introducing a finite displacement between the A and B lattices, e.g., along the $\mathbf{b}_1 = [(4\pi/5), (2\pi/5), 0]$ direction. In Figs. 7(c) and 7(d), we plot energy difference $E_4(\mathbf{k}) - E_3(\mathbf{k})$ of a finite displaced tetragonal moiré crystal. As one can see, the $D_4 \times \mathbb{Z}_2$ symmetry-protected nodal lines are completely gapped by the displacement $\mathbf{d}$. Moreover, there emerge two topological nodal lines (red solid) near the MA axes. These two nodal lines are topologically protected by the remaining $\mathcal{M}_1\sigma_x$

symmetry and have a nonvanishing topological number $\zeta_{\mathcal{M}_1\sigma_x}$ as defined in Refs. [41,46]. If we decrease $|\mathbf{d}|$, the two topological nodal lines keep moving toward the MA axes and finally meet each other and merge into the $D_4 \times \mathbb{Z}_2$ protected nodal lines along MA when $|\mathbf{d}| = 0$.

We have also searched for the possible Weyl points in the tetragonal lattice by introducing a further displacement which breaks the $\mathcal{M}_1\sigma_x$ symmetry. However, for a large range of parameters, we do not see any signature of a nodal point in this tetragonal moiré crystal.